

# Chapter 5

## Model fitting

The photometry described in the preceding chapter is an impressive dataset, in both the breadth and density of its coverage of the optical/NIR spectrum. This, coupled with its quasi-simultaneous nature, makes it an excellent resource for modelling the optical emission of the PHFS quasars. In this chapter we will endeavour to construct physical models for the optical emission that are consistent with the data. Much of the analysis and results presented in this chapter is presented in a paper (Whiting, Webster, and Francis 2001) that is currently in press.

### 5.1 Power law fitting

In searching for physical models, it is usually best to start with the simplest models and work up in complexity. One of the simplest models to fit to data is that of a power law. Francis et al. (2000) found that about 90% of the PHFS have approximately power law SEDs. We first wish to test this more rigorously. As a starting point, we choose to fit (naively) a simple power law, with an unconstrained spectral index. This will separate out the sources that have power law SEDs from those that show some curvature in their spectrum.

This power law can be parametrised as  $f_{PL}(\lambda) = c\lambda^\alpha$ , with the normalisation  $c$  and the spectral index  $\alpha$  free parameters (which will be fit to the data). Note that this model implies  $f_\nu \propto \nu^{-2-\alpha}$ , but we will be working in terms of  $\lambda$  and  $f_\lambda$ .

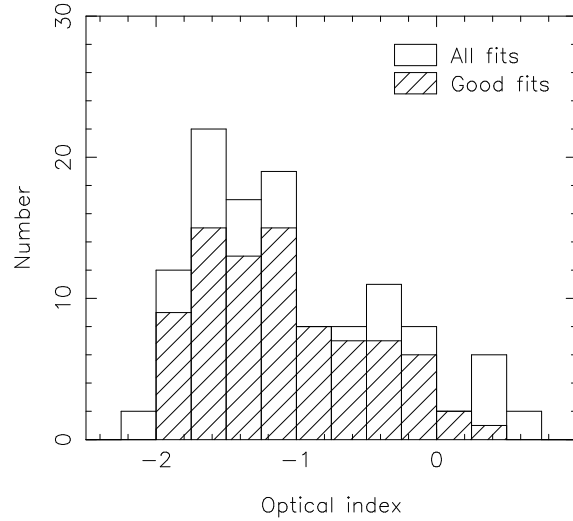


Figure 5.1: Histogram of fitted power law indices. Hatched histogram indicates good fits, while open histogram indicates all fits.

### 5.1.1 Fits to data

To fit this model, the magnitudes in Table B.1 were converted into fluxes according to the zero-magnitude fluxes listed in Table 4.1. This model is fit to these fluxes using a least-squares method. This generates a  $\chi^2$  value:

$$\chi^2 = \sum_{i=1}^7 \frac{(y_i - f_{PL}(\lambda_i))^2}{\sigma_i^2}, \quad (5.1)$$

which indicates the goodness of fit. A fit to a source will be deemed to be “good” when the value of  $\chi^2$  is less than the cut-off value corresponding to the 99% confidence level of the  $\chi^2$  distribution. For a source with 5 degrees of freedom (as is the case for most sources with this power law model), this cutoff level is 15.09. (Note that increasing the value of this cutoff is equivalent to increasing the confidence level – for example, the 99.5% cutoff is 16.75 for 5 degrees of freedom.) If the  $\chi^2$  value is greater than this cutoff level, then the null hypothesis that the power law model fits the data is rejected.

When this power law model is fitted to the data, we find that 83 sources (or 71% of the total) have good fits. The distribution of resulting power law indices, both for the good fits and for all sources, is shown in Fig. 5.1.

The spectral indices of these good fits span a wide range of values. At one extreme there are the sources with relatively blue SEDs ( $\alpha \lesssim -1.4$ ). These sources are characterised by their blue continuum, the presence of moderate to strong emission lines, and generally low X-ray flux (most were not detected by *ROSAT* (Siebert et al. 1998)).

At the other extreme are the sources with redder SEDs (that is, flatter in  $f_\lambda$ ), with  $-1 \lesssim \alpha \lesssim 0$ . These sources are blazar type objects, with high optical polarisation (Wills et al. 1992) – see Section 6.3 – as well as relatively weak (or even absent) emission lines – in fact, all the BL Lac objects in our sample are in this region of the power law index distribution.

### 5.1.2 Interpretation of power laws

So, we have fit a power law to a large majority of the sources in our sample, spanning a wide range of spectral indices. Are the physical processes that generate this power law the same for all sources? That is, does the power law in the blue sources have the same origin as that in the red sources?

The first class of sources – the blue sources – are being fit by a blue power law, which has similar colours to the blue power law emission seen in optically-selected quasars (Francis 1996). This is likely to be the optical part of the continuum emission from the accretion disk (often termed the big blue bump).

However, the power law being fit to the redder sources is most likely of different origin to that seen in the blue sources. These objects exhibit characteristics commonly associated with optical synchrotron emission (such as high optical polarisation and lack of prominent emission lines), and so we postulate that this emission is, at least in part, some form of synchrotron emission. The slope of the power law can then be used to determine  $p$ , the power law index of the electron energy distribution (i.e. defined such that  $N(E) \propto E^{-p}$ : see Chapter 3). Using the values shown in Fig. 5.1, we obtain  $2 < p < 6$  (using  $-1.5 < \alpha < 0.5$  and  $p = 2\alpha + 5$ ).

If synchrotron emission is present in the spectra of at least some of these quasars, then this raises the question “Is the synchrotron component best modelled by this power law?” The synchrotron component will be present in one of two forms, as discussed in Chapter 3: a power law caused by an unbroken (power law) electron energy distribution, or a turning-over component caused by a break or a cut-off in the electron energy distribution.

(Note that the power law can also be produced by a synchrotron spectrum turning over at higher frequencies than those observed.)

Both of these forms can be tested. The power law model must produce power law indices that are consistent with slopes of plausible energy distributions. The presence or otherwise of a turnover can be evaluated by examining the sharpest possible turnover (caused by an abrupt cut-off in the energy distribution at some maximum energy). This will provide the maximum contrast with the power law, and is consistent with modeling done by other authors (for example, Meisenheimer et al. 1996).

Many of the sources, while they have power law fits that can not be rejected at the 99% confidence level, show evidence for curvature in their SEDs. This curvature can be ‘n’-shaped (higher in the middle than at either end), ‘u’-shaped (lower in the middle) or perhaps take the form of an inflection (e.g. the flux decreases, levels off and possibly decreases again). (See Fig. 5.3 for illustrations of the different types.) Most of the sources classed as BL Lac objects are ‘n’-shaped, and so we postulate that these sources are dominated by a synchrotron component that is turning over in the optical.

Other sources, however, are bluer in the optical than in the NIR (i.e. show an inflection, without the turn-up seen in ‘u’-shaped sources). This is a possible indication of the presence of excess emission in the NIR, in addition to a blue power law. We propose that this excess emission is due to a synchrotron component that has turned over in the NIR, and so does not dominate in the optical, where the dominant emission is instead a blue power law similar to that observed in the bluest sources.

## 5.2 Physical models

In response to this phenomenological classification, we next propose the following two-component physical model: one component is a blue power law, representing continuum emission from the accretion disk region; and the second is synchrotron emission, representing emission from the relativistic jet (that is known to be present due to the flat-spectrum radio emission seen in these objects).

### 5.2.1 Accretion disk emission

We have found, from the simple power law fitting, that the bluest sources have power law continua. The slopes of these power laws are consistent with them being the same component as that seen in optically-selected quasars, commonly termed the “Big Blue Bump” (BBB). This component, then, is taken to represent the underlying quasar continuum in the UV-optical part of the rest-frame spectrum – that is, the “un-reddened” quasar continuum.

Over the wavelength range of our observations, the BBB is modelled as a simple power law,  $f_\lambda \propto \lambda^{\alpha_B}$  or  $f_\nu \propto \nu^{-2-\alpha_B}$ . Francis (1996) found the median slope for a subsample of quasars from the Large Bright Quasar Survey (LBQS), taken from optical/NIR photometry, was  $f_\nu \propto \nu^{-0.35 \pm 0.3}$ , and noted that the observations were consistent with an intrinsic continuum slope of  $f_\nu \propto \nu^{-0.3}$  that is reddened by various amounts of dust. We therefore take the value of  $\alpha_B$  to be  $-1.7$ . The effects of allowing the value of  $\alpha_B$  to vary are considered in Section 5.7.

### 5.2.2 Synchrotron emission

#### Rationale

All the PHFS sources are radio-loud flat-spectrum sources, and thus very likely have relativistic jets that emit synchrotron radiation, at least at radio frequencies. Could this synchrotron emission extend up to the optical/NIR part of the spectrum? Our power law fitting from the previous section provides circumstantial evidence for this: the redder sources in the optical tend to be the ones with higher polarisation (a good sign of synchrotron emission) and less prominent emission lines (possibly a sign that the emission lines are being swamped by the presence of a synchrotron component).

As discussed above, the synchrotron spectrum could take the form of either a power law, from a power law distribution of electron energies, or a power law with a break or turn-over, due to an electron energy distribution that exhibits a break or even a cut-off. These types of spectra are discussed in Chapter 3. The latter type of spectrum is seen in optical synchrotron jets (see Section 2.2.1 and references therein), where the optical spectrum is like  $\nu^{-1.2}$ – $\nu^{-3.0}$ , compared to a radio–optical spectrum of  $\nu^{-0.6}$ – $\nu^{-1.0}$ .

Additionally, a synchrotron spectrum that has a turn-over will, when combined with the blue power law, be able to reproduce an inflection-like

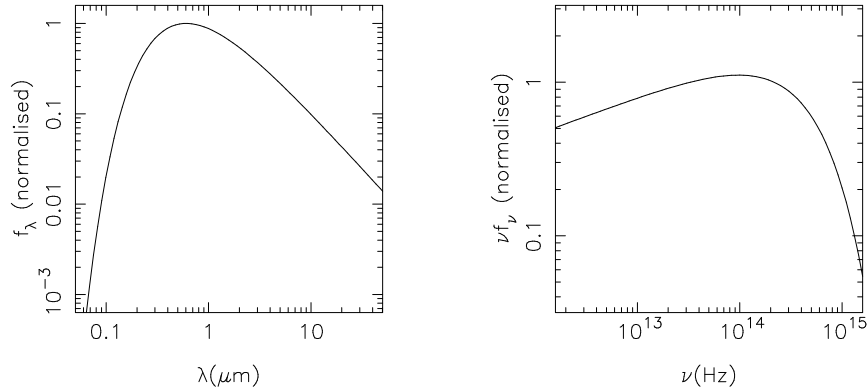


Figure 5.2: The synchrotron model used in the analysis, in both  $f_\lambda$  and  $\nu f_\nu$  units. Both plots have been normalised so that the peak flux in  $f_\lambda$  is 1. Note that the vertical scale is different in the two plots.

SED, which is seen in a number of the PHFS sources. Also, such a spectrum, particularly in the region of the turn-over, will be quite red, and will thus be able to account for the red colours of many of the SEDs.

### Analytic modelling

We consider here synchrotron emission from a population of electrons with an energy distribution that has the form of a power law up to some maximum energy and zero beyond this (i.e. an energy spectrum with an abrupt cutoff, as modelled in Section 3.3). This can be expressed as a distribution of the Lorentz factor  $\gamma$  of the radiating electrons:

$$N(\gamma) d\gamma = \begin{cases} \kappa \gamma^{-p} d\gamma & 1 \leq \gamma \leq \gamma_+ \\ 0 & \gamma > \gamma_+ \end{cases}$$

This is consistent with modelling done by Meisenheimer et al. (1996) on the jet of M87. They found that the overall synchrotron spectrum of the brightest parts of the jet was best described by a spectrum that had a sharp cutoff at  $\nu_c \approx 10^{15}$  Hz, and modelled this with an energy distribution of the form of a straight power law  $N(\gamma) \propto \gamma^{-2.31}$ , with a rather abrupt high energy cutoff. We consider the effect of using a power law synchrotron spectrum without a cutoff in Section 5.5.

Such a synchrotron spectrum is straightforward to model analytically.

We use the synchrotron model from Section 3.2, for the case of a disordered field. This model is somewhat more general than the ordered field model, and the wavelength dependence of the two are the same. The single particle luminosity for a radiating electron is given by

$$L_{1p}(\omega) = \frac{\sqrt{3}e^3 B \sin \theta}{8\pi^2 \epsilon_0 c m_e} F(x)$$

where  $\omega = 2\pi\nu$  is the angular frequency, and  $F(x)$  is given by Eqn. 3.6. Since we are interested in the luminosity of a population of particles, so we need to integrate  $L_{1p}(\omega)$  over suitable distributions of energies and pitch angles. The energy distribution is that given above, while the pitch angle distribution that we use is an isotropic one, where the probability distribution is  $p(\theta)d\theta = \frac{1}{2} \sin \theta d\theta$ . Thus, the integrated luminosity from such a population is

$$L(\omega) = \frac{\sqrt{3}e^3 B \kappa}{16\pi^2 \epsilon_0 c m_e} \int_0^\pi \sin^2 \theta \left( \int_1^{\gamma_+} \gamma^{-p} F(x) d\gamma \right) d\theta$$

An example of such a spectrum is shown in Fig. 5.2, for  $\gamma_+ = 10^6$  and  $B = 10^{-8}\text{T} = 10^{-4}\text{G}$  (the value of  $\kappa$  has been taken to be 1). The peak frequency  $\nu_c$  depends on these two values, and can be shown by simple arguments (Blandford 1990) to be approximated by  $\nu_c \sim \gamma_+^2 B$  MHz (where  $B$  is measured in Gauss).

The slope of the power law tail (at frequencies  $\nu \ll \nu_c$ ) is related to the energy power law index by  $\alpha_S = (p - 5)/2$  (where  $f \propto \lambda^{\alpha_S}$ ). The energy distribution for the spectrum in Fig. 5.2 is taken to be  $N(\gamma) \propto \gamma^{-2.5}$  (i.e.  $p = 2.5$ ), giving a power law of  $f_\lambda \propto \lambda^{-1.25}$ .

We consider here a range of  $p$  values from  $p = 2.0$  to  $p = 3.0$ , which gives a range of long-wavelength power law slopes of  $\alpha_S = -1.5$  to  $\alpha_S = -1.0$ . This range covers the distribution of radio-to-optical slopes for the PHFS sources (this distribution can be seen in Fig. 7.7c), as well as the distribution of radio-to-optical slopes observed in optical synchrotron jets (i.e.  $\nu^{-0.5}$  to  $\nu^{-1.0}$ : see Table 2.2 or Scarpa and Urry (2001)). Allowing  $p$  to vary does not significantly alter the results of our analysis – see Section 5.7 for further discussion.

We also note here that a value of  $p > 3$  means that the  $\nu f_\nu$  flux will increase towards longer wavelengths (since  $f_\nu \propto \nu^{-(p-1)/2}$  and so  $\nu f_\nu \propto \nu^{-(p-3)/2}$ ) and this results in the radio flux being severely overestimated by

the fitted synchrotron component, since observationally the radio emission always has a lower  $\nu f_\nu$  flux than the optical. This assumes that the same synchrotron component is responsible for both the optical and radio emission, which is an assumption commonly made, particularly for the modelling of optical synchrotron jets (Meisenheimer et al. 1996).

### 5.3 Fitting technique

These two components (the blue power law and the synchrotron component) are combined linearly to form a model  $f_C(\lambda) = a\lambda^{-1.7} + bf_{synch}(\lambda)$  that is fit to the data in the same way as the power law model (that is, minimising the  $\chi^2$  value as given by Eqn. 5.1). The reduced  $\chi^2$  value (that is,  $\chi^2/\nu$ ) for each of the two models (combined and power law) are compared, and the model with the lowest  $\chi^2/\nu$  is chosen to be the best fit model. Here,  $\nu$  is the number of degrees of freedom. This is defined as the number of data points minus the number of parameters in the fit.

In fitting the combined model, the location of the peak wavelength of the synchrotron spectrum,  $\lambda_p$ , was allowed to vary. This variation was allowed to occur over a range of rest frame wavelengths, such that the curvature of the spectrum caused by the turn-over affected the synchrotron flux in the region of the data points (in other words, we did not want to just be fitting the power law part of the synchrotron spectrum). Quantitatively, the minimum peak wavelength was taken to be half a decade shorter than the  $B$  band ( $0.44\mu\text{m}$ ) shifted to the rest frame, and then 20  $\lambda_p$  values per decade (evenly spaced in  $\log_{10} \lambda_p$ ) were considered, up to a maximum peak of  $10\mu\text{m}$ . For each of these synchrotron functions, a best fit to the data was found, and then the best of these was chosen, giving the best fit  $\lambda_p$  value for that source.

A selection of fits are shown in Fig. 5.3, for sources best fit by a range of both power law and combined models. Fits for all the sources are shown in Appendix D.

### 5.4 Results

This section discusses the results and implications of the fitting, from the point of view of the different parameters and variables.

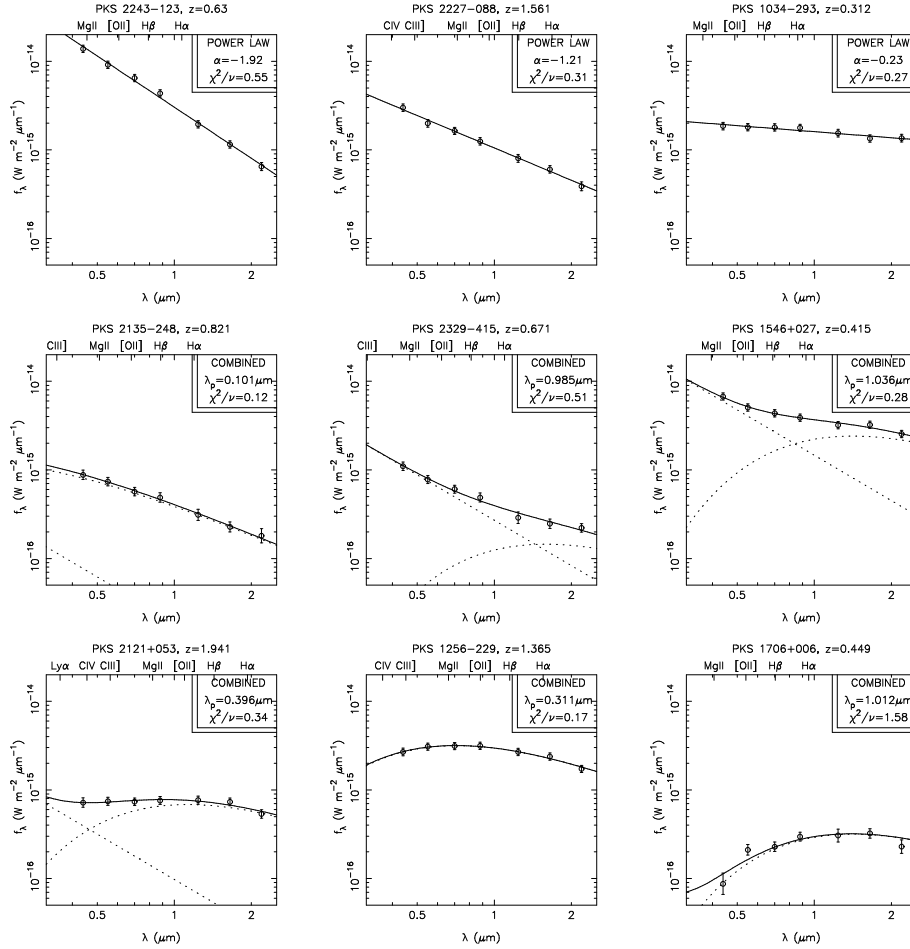


Figure 5.3: Examples of the various types of photometry, and the fits to them. The horizontal axis on each plot is wavelength, in  $\mu\text{m}$ , and the vertical axis is  $f_\lambda$  in  $\text{W m}^{-2} \mu\text{m}^{-1}$ . Error bars on the fluxes are  $1\sigma$ . The locations of notable emission lines are shown, based on the redshift of each quasar. For the combined fits, the individual components – the power law ( $\alpha_B = -1.7$ ) and the synchrotron component ( $p = 2.5$ ) – are shown as dotted lines. The  $\lambda_p$  value, where given, is for the quasar rest frame. See Appendix D for the complete set of sources and their fits.

### 5.4.1 $\chi^2/\nu$ distributions

The combined model was fit to the data in the method detailed above, and the fits were compared to those of the power law model. The best fitting model (based on the  $\chi^2/\nu$  values) was chosen for each source. For the “default” values of the model parameters ( $p = 2.5$  and  $\alpha_B = -1.7$ ), we find that 93 sources (or 79% of the total) are well fit by one of the models. Of these, 48 are best fit by the power law model, and 45 by the combined model. The results for each source are summarised in Table C.1, which gives, for those sources with good fits, the  $\chi^2/\nu$  values for each models, as well as the power law index, synchrotron peak wavelength ( $\lambda_p$ ) and the ratio of synchrotron to total flux at a rest-frame wavelength of  $0.5\mu\text{m}$ .

The first result to look at is the distribution of  $\chi^2/\nu$  values, as this will give a good indication of how good the fits are for each model, and how the two models compare to each other. Fig. 5.4 shows the distributions of  $\chi^2/\nu$  values for all sources, divided on the basis of which model fit each source best. It also shows the distribution of best-fit  $\chi^2/\nu$  values for all sources. As can be seen, the distribution for the sources best fit by the combined model is noticeably broader than that for the power law sources, with more sources having very low  $\chi^2$  values.

To directly compare the two models, one can plot, for each source, the fitted  $\chi^2/\nu$  from each model against one another. This is done in Fig. 5.5, where the resulting best fit is indicated by the symbol used. The colour of the point indicates the power law index from the power law model fit. Two points can be drawn from this plot. Firstly, those sources best fit by the combined model tend to be a long way from the line of equality – that is, when the combined model is fit best, it is generally much better than the power law model. These are the sources that exhibit significant curvature in their SEDs. Secondly, the bluer sources tend to be best fit by the power law model, while the intermediate and redder sources are more likely to be best fit by the combined model. We note that the power law model has one more degree of freedom than the combined model, and so a source with equal  $\chi^2$  for both models will give a slightly lower  $\chi^2/\nu$  for the power law model.

So, one can see that the blue sources are most likely to be best fit by the power law, but not by a big margin, indicating that the two models give very similar fits. This indicates that the assumption of the presence of a power law in the combined model is accurate, as it is this power law that

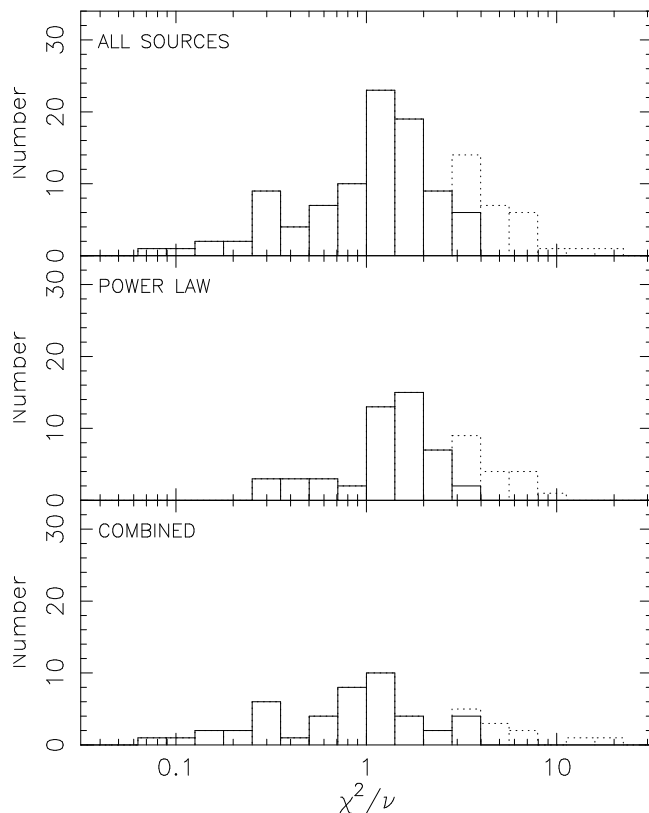


Figure 5.4: Histograms of the reduced  $\chi^2$  values, for all sources and for each of the best-fit models. The dotted histogram shows those sources whose fits are rejected at the 99% confidence level.

means the combined fits are close to the power law fits (which in turn means that the points are close to the line of equality on Fig. 5.5).

### 5.4.2 Synchrotron components

The properties of the synchrotron components that are fitted as part of the combined model are of particular interest. As can be seen in Fig 5.6, the peak wavelengths are restricted to a relatively narrow range of values (approximately a decade in wavelength). However, this is likely to be largely a reflection of the distribution of the wavelengths of the photometric points.

The strength of the fitted synchrotron component varies considerably from source to source. In Fig. 5.7, the ratio of the synchrotron and power law components at a rest-frame wavelength of  $0.5\mu\text{m}$  is shown for all sources best fit by the combined model. The main bulk of this distribution spans nearly

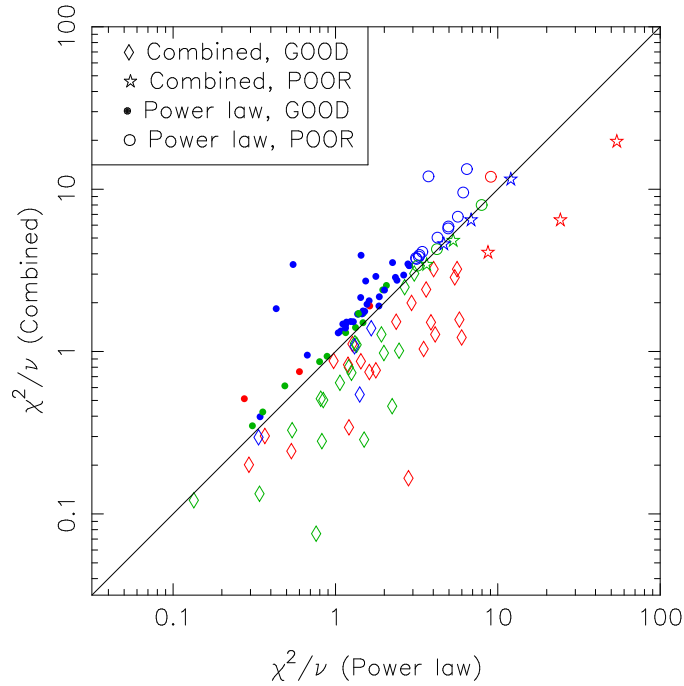


Figure 5.5: Comparison of the  $\chi^2/\nu$  values for the power law model and the combined model. The symbols indicate which source fits best, and whether that fit is accepted at the 99% confidence level. The colours of the points indicate the slope of the power law from the power law fit (regardless of whether that fit was the best or not): red –  $-\alpha > -0.5$ ; green –  $-1.3 < \alpha < -0.5$ ; blue –  $-\alpha < -1.3$ . The line shown is the line of equal  $\chi^2/\nu$ .

four orders of magnitude. This large range of values, which is also seen in the normalisations of the individual components, indicates that a continuum of variations of these components is seen, probably due to variations in the strengths of the inner jet and emission from the accretion disk and/or surrounding regions.

We also note that a small number of the sources at the high-ratio end of the distribution are faint, red sources, that are likely to be significantly dust-reddened. They are thus fit with a dominant synchrotron component, as the synchrotron spectrum has the approximate form of a power law with an exponential cut-off (which is the same as a power law with dust extinction).

### 5.4.3 Power law sources

While many sources have been fitted better with the combined model, a large number are still preferentially fit with the power law. If we plot a

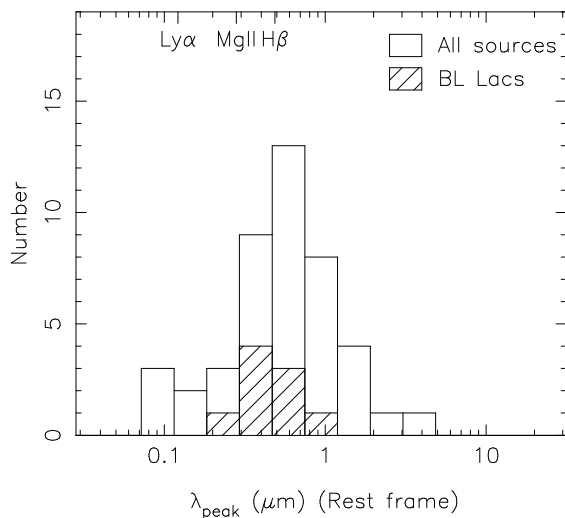


Figure 5.6: Histogram of peak wavelengths, showing all sources fit best with the combined model, in the rest frame. The solid histogram shows all sources with combined fits accepted at 99% confidence, while the hatched histogram shows the BL Lac objects. The locations of three prominent emission lines are given for reference.

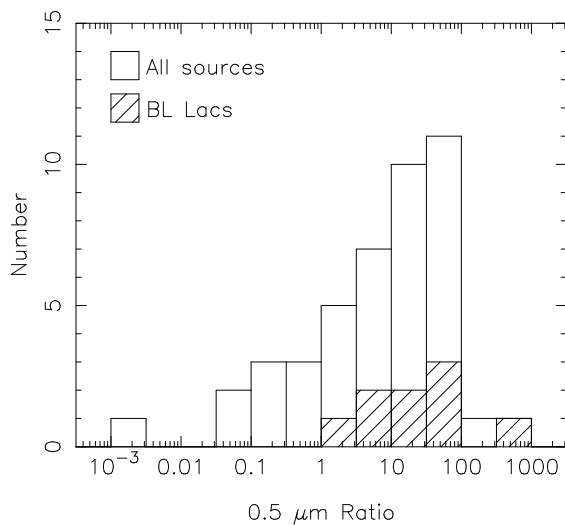


Figure 5.7: Histogram of ratios of the synchrotron component to the power law component of the combined model, for those sources best fit by the combined model. The ratio is calculated at a rest-frame wavelength of  $0.5\mu\text{m}$ . The hatched histogram shows the BL Lac objects.

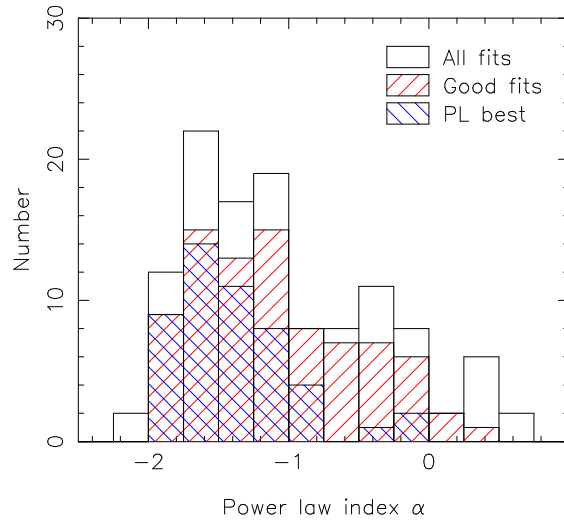


Figure 5.8: Distributions of the fitted power index  $\alpha$ . The open histogram shows all 117 sources, the hatched histogram shows which of those fits are accepted at 99% confidence, while the cross-hatched histogram shows which of those sources have power law fits better than the combined fit.

histogram (Fig. 5.8) of the power law indices of those still fit by the power law model, it can be seen that most of those sources that are preferentially fit by the power law model are the bluer sources, while the majority of the sources with indices  $\alpha > -1$  are fit better by the combined model.

It is worth noting here that there are a significant number of power law sources with what might be termed “intermediate” slopes (that is, slopes with  $\alpha \sim -1.2$ , which are redder than the blue power law from the combined model) and a few red ( $\alpha > -0.5$ ) sources. These latter sources are often high polarisation sources (see Chapter 6), and so are likely to be synchrotron dominated (they of course show no evidence for a turn-over similar to that being fit by the synchrotron model, although their slope could be due to a very steep energy distribution (i.e. large  $p$ ) or a more gradual turn-over).

The presence of the intermediate power law slopes raises interesting issues. Are similar sources seen in optical quasar surveys? Fig. 5.9 shows the power law index distributions for the sources best fit by the power law model, together with the LBQS quasars from Francis (1996). While the two data sets cannot be said to come from different parent distributions (the Kolmogorov-Smirnov test probability for the null hypothesis that the parent distributions are the same is 11.3%), there does appear to be an excess

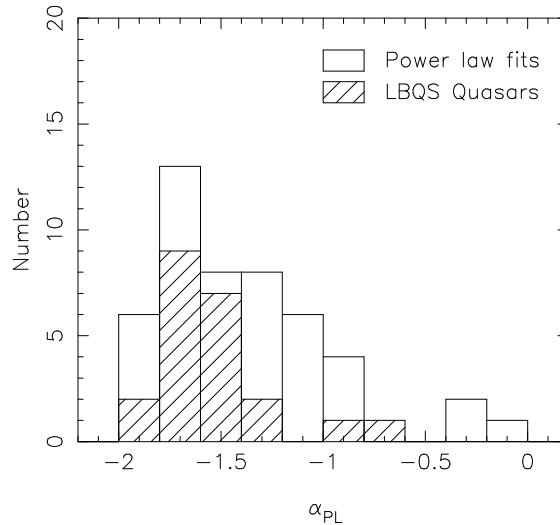


Figure 5.9: Histograms of power law indices for the power law sources in this paper and for the LBQS quasars from Francis (1996).

of quasars in our sample for  $-1.4 \lesssim \alpha \lesssim -0.8$ . This may indicate that the accretion disk emission in radio loud quasars has a broader range of colours, which would have implications for models of accretion disk emission. This effect may be related to the interaction between the jet outflow and the disk.

#### 5.4.4 Redshift distributions

To give an indication of what sources are being fit by which model, Fig. 5.10 shows the redshift distributions of the sources best fit by both the combined model and the power law model.

The two distributions are different at the 99.9% level, with the average redshifts being  $z = 1.51$  (power law sources) and  $z = 0.90$  (combined model sources). The combined model tends to fit sources at lower redshift, while the higher redshift sources are nearly always fit by the power law model. For example, of the 17 sources with  $z > 2$ , only three are best fit by the combined model, compared with 12 out of the 18 sources with  $z < 0.5$ .

This may be an indication of the fact that the fixed observation band ( $0.4\mu\text{m}$  to  $2.5\mu\text{m}$ ) corresponds to different rest frame wavelength ranges at different values of  $z$ : at  $z = 0.5$  this is  $0.27\mu\text{m}$  to  $1.67\mu\text{m}$ , while at  $z = 2.5$  it is  $0.11\mu\text{m}$  to  $0.71\mu\text{m}$ . This shorter wavelength pass-band will result in less synchrotron emission being observed, due to the turnover of the synchrotron

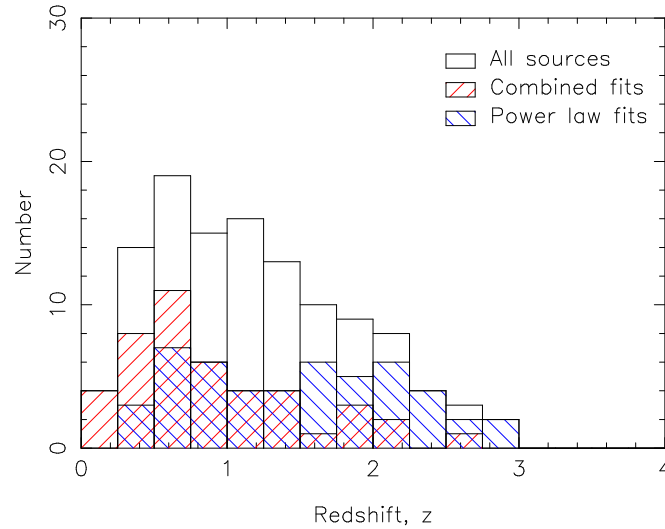


Figure 5.10: Redshift distributions of sources best fit by each model. The redshift distribution of all sources that had models fit to them is also shown for comparison.

component. If this is the case, this is evidence that there is an upper limit to the distribution of  $\lambda_p$  values, in the sense that there are fewer sources with  $\lambda_p$  short enough to give significant synchrotron emission in the redshifted pass-band.

This is reminiscent of the observation made in Section 2.2.1 that, despite being preferred by selection, almost no jets are seen in AGN with their synchrotron spectra extending up to X-ray energies. This indicates that the optical region is about as energetic as significant synchrotron emission from AGN/quasar jets can get.

We also note that, as well as this effect, the shorter rest frame wavelengths that are observed will result in a stronger big blue bump (should one be present), and so even if the synchrotron were the same level, its relative strength will be decreased.

#### 5.4.5 Colour-colour diagram

Finally, the consistency of the model fits can be checked by plotting the sources on a colour-colour diagram. An optical colour vs. NIR colour diagram was used by Francis et al. (2000) to graphically show the range of different SEDs present amongst the sample. In Fig. 5.11 the  $J - K$  colours of all sources that have good model fits are plotted against their  $B - I$  colours.

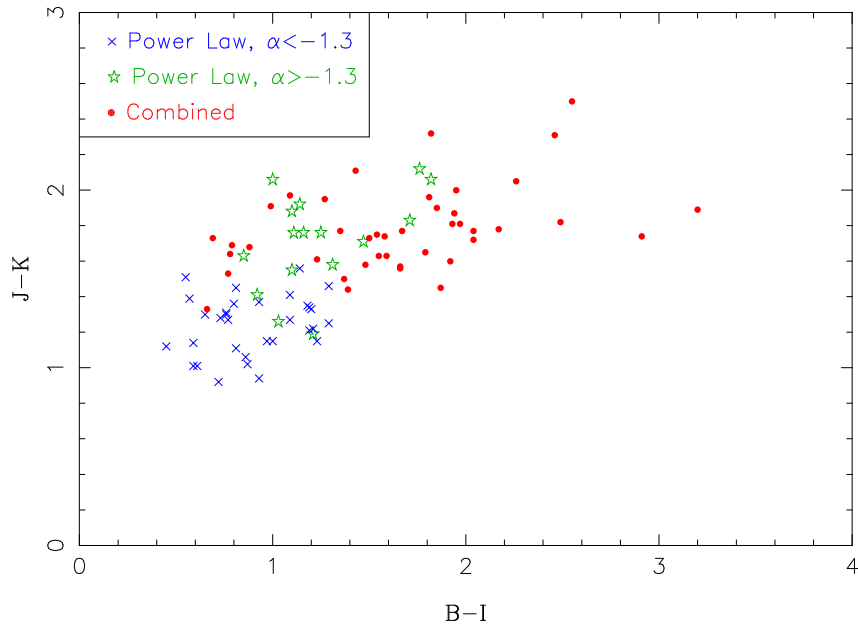


Figure 5.11: Infrared ( $J - K$ ) colour versus optical ( $B - I$ ) colour for all quasars with good model fits. The best fit model is indicated by the symbol used.

The sources are also separated into their fitted model types, with the power law sources divided into red and blue power laws according to their fitted slope (using  $\alpha = -1.3$  as the dividing line).

Clear distinctions can be made between the different model types. The blue power law sources lie at the bottom left corner, indicating blue colours in both optical and infrared, while as the power law becomes redder, the sources move towards the upper-right. Many of the combined fits are in the optically-red region of the plot, indicating that the SED is turning over in the optical (similar to 1256–229 in Fig. 5.3, for example). The reddest sources in  $B - I$  are sources with optical continua that drop towards the blue, in the manner of 1706+006 (see Fig. 5.3), which are typical of dusty sources, or sources dominated by host galaxy emission, and are fit by a dominant synchrotron component. Note that 1706+006 is the faintest of the sources shown in Fig. 5.3, and is a good candidate for dust extinction. Other combined sources, however, are among the bluer sources in the optical, but have redder NIR colours than the power law sources. These are the sources that show an inflection, similar to 2329–415 in Fig. 5.3, where the synchrotron component is dominant in the NIR but turns over and has less

effect in the optical.

## 5.5 Other models: Power law synchrotron

Thus far, we have been considering a synchrotron model that peaks at some  $\lambda_p$  and then turns over sharply (i.e. exponentially). This model was chosen for consistency with other modelling done for optical synchrotron emission (Meisenheimer et al. 1996), and to provide the maximum contrast with the power law model. However, synchrotron emission could alternatively be present in the form of a power law. What if we consider a model of the same form as the combined model, but with this power law synchrotron model instead? Is this any better at fitting the observations?

Such a model was constructed, being a linear combination of the blue (BBB) power law from earlier, and a power law of variable index:  $f(\lambda) = a\lambda^{-1.7} + b\lambda^{\alpha_S}$ . To distinguish it from the BBB power law, the indices were restricted to the range  $-1.6 < \alpha_S < 1.5$ . This model was then fitted to the photometry in the same way as previously. Note that the special case of  $a = 0$  is simply the power law fit from Section 5.1 (with the index restricted to lie in the above range).

We do note, briefly, that by restricting the index of this power law to lie in the above range, we are imposing an implicit bias against fitting blue synchrotron power laws. Should there be any synchrotron spectra with a slope bluer than  $\lambda^{-1.5}$ , this fitting routine will not fit them correctly (although such slopes are bluer than any of the observed radio-to-optical slopes seen in the PHFS sources – see Fig. 7.7c). However, due to the nature of the fitting routine, this cannot be remedied (if the routine tries to fit two power laws of too similar slopes, it will reach a singularity and fail to work).

The  $\chi^2/\nu$  values for this model are plotted in Fig. 5.12 against those for the combined model detailed in Section 5.2. The symbols used indicate which model is preferred, and whether it is a good or bad fit. For sources that are bluer than  $\lambda^{-1.7}$ , the best fit is always with no synchrotron component (for both forms of the synchrotron model), as the presence of the second component will redden the blue power law. Hence, for these sources, both the original combined model and the two power law model give the same fit, consisting of just the  $\lambda^{-1.7}$  (i.e. BBB) power law. These sources are indicated by the “Equal fit” symbols on Fig. 5.12.

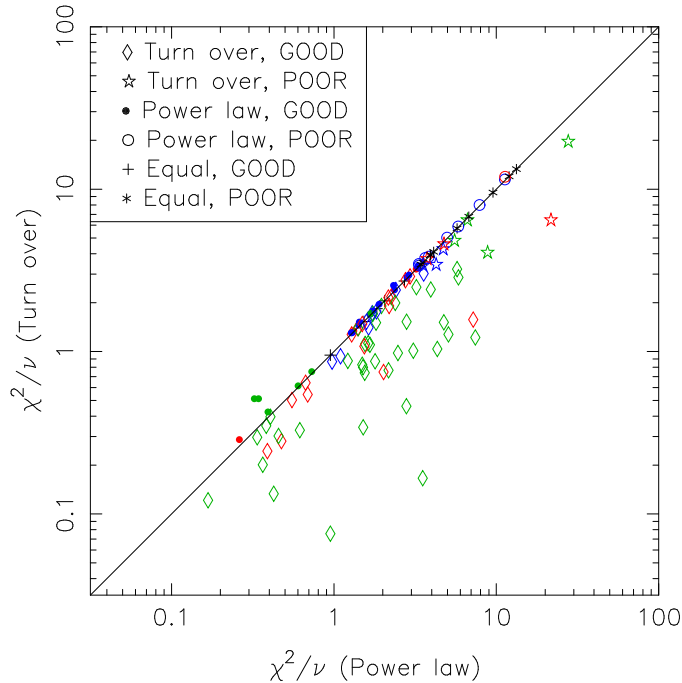


Figure 5.12: Values of  $\chi^2/\nu$  for the combined models featuring either power law synchrotron models or synchrotron models with a turn-over. The symbols relate to which model is preferred, and whether the fit is accepted at the 99% confidence limit or not (i.e. good or poor). The line shown is the line of equal  $\chi^2/\nu$ . The colours relate to the location of  $\lambda_p$  from the fit with the turn-over synchrotron model: red –  $\lambda_p > 1\mu\text{m}$ ; green –  $0.1\mu\text{m} < \lambda_p < 1\mu\text{m}$ ; blue –  $\lambda_p < 0.1\mu\text{m}$ .

The power law synchrotron model obviously does not do as well at explaining the optical/NIR SEDs of the quasars as the model with a turn-over. Only 22 sources have a good power law synchrotron fit that is better than their fit from the synchrotron model with a turn-over, and only two of these (1034–293 and 2329–415, with indices of  $\alpha_S = -0.21$  and  $\alpha_S = 0$  respectively) are significantly better. These power law synchrotron sources may have turn-overs at shorter wavelengths, beyond our currently available data. The only way to tell would be to obtain UV photometry (ideally contemporaneous with the optical/NIR).

We note that many of the sources from Fig. 5.8 that are in the cross-hatched histogram (that is, had better single power law fits than combined fits) and had  $\alpha > -1.6$ , also had fits with the two power law model that were better than those with the turnover synchrotron model. (This is not always the case, however, since going from one power law to two decreases

the degrees of freedom, so the  $\chi^2/\nu$  value will be greater.) In most of these cases, the blue power law (the  $\lambda^{-1.7}$  component) is either absent or has a very low normalisation.

For most sources, however, the synchrotron model with a turn-over gives a much better fit to the observed optical/NIR SEDs (many of these sources show large ratios of synchrotron to blue power law flux). This result provides clear evidence that there is a break or a cutoff present in the energy distribution of the radiating particles. Additionally, it shows that there are few, if any, sources with turn-overs at shorter wavelengths (i.e. in the UV or X-ray). This is in accord with the finding from the redshift distributions (see the discussion in Section 5.4.4).

## 5.6 Other models: Hot dust

So far, it has been shown that, for a number of sources, the optical–NIR photometry is well fit with a power law plus a curved component, which we have assumed to be the turnover of a synchrotron component. However could another model be used instead of synchrotron? One possible alternative is blackbody emission resulting from hot dust.

To test this model, we used a blackbody emission spectrum due to dust at a temperature of 1750 K (the sublimation temperature characteristic of dust grains consisting of graphite and silicates, e.g. Laor and Draine (1993)) emitted in the quasar’s rest frame. A blackbody curve at this temperature would have its peak, in the quasar rest-frame, at  $1.66\mu\text{m}$ . This blackbody spectrum was combined with the same  $\lambda^{-1.7}$  power law used in the combined model to produce a model that was fit to the data.

The fits generated by this model were almost always worse than those of the synchrotron model, as seen in Fig. 5.13. This was due to the peak of the blackbody occurring at much longer observed wavelengths than the  $K$  band. Discounting the case where only the  $\lambda^{-1.7}$  component was fit (the “Equal” points in Fig. 5.13), in only 12 cases was the  $\chi^2/\nu$  value from the dust model less than that of the synchrotron model, and in most cases this was because the dust model had one more degree of freedom. For each of these objects, the SED took the form of a blue power law (one object was  $\lambda^{-1.4}$ , and the rest were bluer than  $\lambda^{-1.54}$ ) that had a slight amount of reddening at the  $H$  and  $K$  bands, which was fit by the presence of the dust blackbody

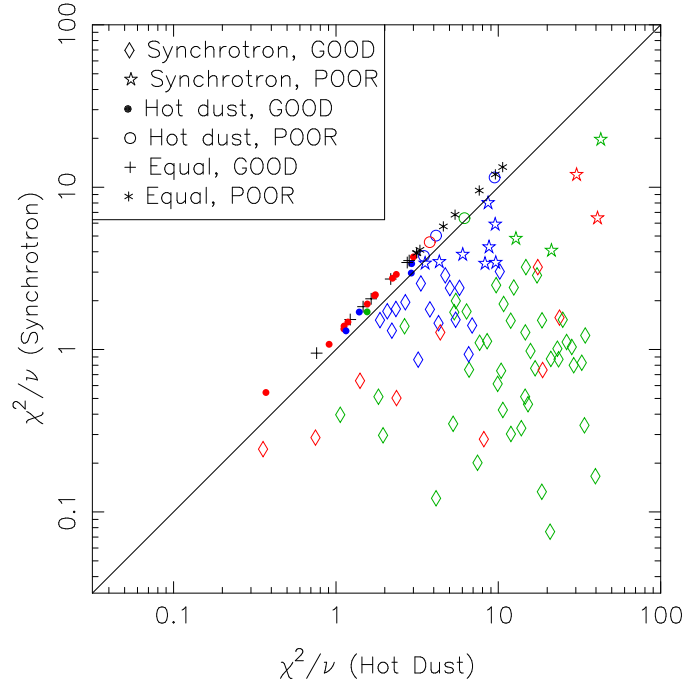


Figure 5.13: Values of  $\chi^2/\nu$  for the combined models featuring either a synchrotron model or a hot dust model. The symbols relate to which model is preferred, and whether the fit is accepted at the 99% confidence limit or not (i.e. good or poor). The line shown is the line of equal  $\chi^2/\nu$ . The colours relate to the location of  $\lambda_p$  from the synchrotron model fit: red –  $\lambda_p > 1\mu\text{m}$ ; green –  $0.1\mu\text{m} < \lambda_p < 1\mu\text{m}$ ; blue –  $\lambda_p < 0.1\mu\text{m}$ .

curve (in other words, the synchrotron fit had a long-wavelength peak, as evidenced by the colour of the points in Fig. 5.13). For the majority of the sources, however, the hot dust model was a lot worse than the synchrotron model, and so can not provide the peak in the optical/NIR that is required to explain many of the observed SEDs.

A number of authors (for example, Sanders et al. 1989, and references therein) have argued for the existence of a near-IR bump, somewhere around  $3\mu\text{m}$ , corresponding to blackbody emission from hot dust. Sanders et al. also mention the presence of a local minimum at  $1\mu\text{m}$ , which they note for its “universality” in their sample of bright quasars from the Palomar-Green (PG) survey. They interpret this to be due to the finite sublimation temperature of dust, causing a drop in the blackbody emission, combined with the rise in flux of thermal emission from hot ( $T \gtrsim 10,000\text{K}$ ) gas. However, any dip observed in the data presented here occurs at wavelengths

which are too short to be attributed to hot dust. To observe a  $1\mu\text{m}$  dip, photometry at longer wavelengths would need to be used.

## 5.7 Alternative parameter values

Throughout this chapter, we have used values for the electron energy index of  $p = 2.5$ , and for the BBB spectral index of  $\alpha_B = -1.7$ . We consider here the effect that changing these values has on the results. Table 5.1 lists the numbers of sources best fit by each of the two models, for each set of parameters, as well as the total number of sources fit by one of the models.

Reducing the value of  $p$  means that the synchrotron spectrum has a bluer slope, which enhances the effect of the turn-over. Using a lower value of  $p$  in the combined model results in some sources, otherwise fit by the power law, being instead fit by the combined model. This is indeed seen in Table 5.1, where the number of sources fit by a power law decreases as you move from  $p = 3$  to  $p = 2.5$  to  $p = 2$  (if the value of  $\alpha_B$  is kept constant), while the number of sources fit by the combined model increases. Note also that more sources have good fits for the lower values of  $p$ .

The  $\lambda_p$  distributions are also affected by a changing  $p$  value. For lower  $p$  values, there are more sources with shorter  $\lambda_p$  values (that is, close to  $0.1\mu\text{m}$ ). This is due to the slope of the power law tail of the synchrotron spectrum: for higher  $p$  values the slope is redder, and so a synchrotron spectrum peaking around  $0.1\mu\text{m}$  would contribute too much at the longer wavelengths.

For the spectral index of the blue optical power law used in the combined model, we considered both steeper and flatter values than the one mentioned in Section 5.2.1. The dispersion found by Francis (1996) for the slopes of LBQS quasars is  $\pm \sim 0.3$ , and so we consider here slopes in  $f_\lambda$  of  $\alpha_B = -1.4$  and  $\alpha_B = -2.0$ .

Changing the slope of this power law (while keeping  $p$  constant) has a much less drastic effect than changing the value of  $p$ . As the slope becomes steeper in  $f_\lambda$  (that is, bluer), only a couple of sources fit by the power law change to be fit by the combined model. The distribution of  $\lambda_p$  values is not changed considerably by the variation of the  $\alpha_B$  values.

In summary, reasonable changes to the fiducial values of  $\alpha_B$  and  $p$  make little difference to the fits, both in the  $\lambda_p$  distribution and the numbers fitted

by each model, although the difference will be accentuated if the values of  $\alpha_B$  and  $p$  are both taken to extremes.

## 5.8 Fits to excluded sources

As explained in Section 4.6, there are a number of sources that were excluded from the sample. Some of these were excluded for the sole reason that they did not have a measured redshift (i.e. those sources with “no  $z$ ” in the final column of Table B.2). These sources are generally quite red and optically faint (thus explaining their undetermined redshift), with the exception of the BL Lac object 0048–097, which has a power law SED. The models were fitted to the observed wavelengths of these objects, to investigate the bias created by excluding them. Note that this fitting does not take into account the change in shape of the synchrotron spectrum due to the redshift of the source. The results are summarised in Table 5.2.

As can be seen, all but three of the sources are fit with the combined model, and the three that aren’t are fit with quite red power laws (that is, red compared to the power laws fit to the sources with measured redshifts). The location of the peak wavelengths are generally into the NIR, which are longer than the bulk of the distribution of the sources with redshifts (see Fig. 5.6). Also, the synchrotron component that is fitted is generally fairly dominant, as evidenced by the fraction values  $F_{0.5}$ . However, it is unlikely that many of these sources would truly be synchrotron sources, since they show more the characteristic shape of dust absorption and are quite faint in the optical (again, with the exception of 0048–097, which was fit with the power law tail of a dominant synchrotron model). We propose that these sources are dust-dominated rather than synchrotron-dominated.

## 5.9 Effect of emission lines on photometry.

As mentioned in Section 4.5, the presence of a strong emission line in the wavelength range of one of the filters will raise the SED level above that of the continuum, which will increase the systematic error in the photometry.

To test this effect, and to see how the fits to the photometry are affected, we examined several sources whose spectra showed significant emission lines. To calculate the contribution of the emission line, we define the total flux in

$p$	2.0	2.0	2.0	2.5	2.5	2.5	3.0	3.0	3.0
$\alpha_B$	-1.4	-1.7	-2.0	-1.4	-1.7	-2.0	-1.4	-1.7	-2.0
Power law	46	44	45	49	48	48	53	52	52
Combined	49	51	50	44	45	44	39	40	40
Total	95	95	95	93	93	92	92	92	92

Table 5.1: Number of sources fitted best by each model, for different values of the parameters  $p$  and  $\alpha_B$ . Only those fits accepted at the 99% confidence level are shown. Values of the parameters used are  $p = 2.0$ ,  $p = 2.5$  and  $p = 3.0$ , as well as  $\alpha_B = -1.4$ ,  $\alpha_B = -1.7$  and  $\alpha_B = -2.0$ .

Source name	$B$ (mag)	$B - K$	Best fit model	$\alpha$	$\lambda_p(\mu\text{m})$	$F_{0.5}$	good/bad fit
0048-097	16.12	3.61	Combined	-	0.15	0.97	good
1110-217	24.41	7.67	Combined	-	1.85	0.88	good
1156-094	21.95	5.08	Combined	-	1.04	0.69	good
1648+015	21.87	5.31	Combined	-	1.17	0.82	bad
1732+094	$B > 23.5$ , $V = 21.15$	$> 7.13$	Power law	-0.39	-	0.00	bad
2056-369	$V > 23.5$ , $R = 23.45$	$> 5.39^*$	Power law	0.59	-	0.00	good
2245+029	21.71	6.22	Combined	-	1.85	0.41	good
2337-334	22.93	6.54	Power law	0.36	-	0.00	good
2344-192	23.52	6.27	Combined	-	1.65	0.83	bad

Table 5.2: Fitting results for sources that were excluded from the sample purely due to their undetermined redshift. The best fit model is given along with either the peak synchrotron wavelength (for combined fits) or the power law index (for power law fits).  $F_{0.5}$  denotes the fraction of the total flux made up by the synchrotron component, at an observed wavelength of  $0.5\mu\text{m}$ . Note that a \* denotes a  $V - K$  measurement, not  $B - K$ , since a  $B$  measurement was not made (due to the faintness of the source).

the line as  $F_{\text{line}}$  and the total continuum flux *under* the line as  $F_{\text{cont}}$ . Then the change in magnitude is given by

$$\begin{aligned}\Delta m &= 2.5 \log_{10} \left( \frac{F_{\text{line}} + F_{\text{cont}}}{F_{\text{cont}}} \right) \\ &= 2.5 \log_{10} \left( \frac{W_{\lambda} + \Delta\lambda}{\Delta\lambda} \right)\end{aligned}$$

where  $W_{\lambda}$  is the equivalent width of the line, and  $\Delta\lambda$  is the wavelength range over which the flux is measured. The equivalent widths and fluxes were computed using the *splot* routine in the data reduction package IRAF.

Note that we are able to do this analysis only for a small number of sources, as not all sources have spectra, and those spectra that do exist are often poor quality, and in all cases non-simultaneous.

The values of the change in magnitude, when considered over the same wavelength range as that of the broad-band filters ( $\Delta\lambda \sim 1000 - 2400 \text{ \AA}$  for the optical bands), ranged from 0.05 – 0.25 magnitudes. By artificially reducing the flux in the relevant band by this amount, the change in  $\chi^2$  due to the presence of the emission line could be evaluated. This was done for several sources that had strong emission lines present in their spectra (the spectra for a large number of PHFS sources will be presented elsewhere (Francis et al. 2001)). A few specific examples are listed here, and are shown in Fig. 5.14 (with the adjusted photometry in red):

- H 1510–089 has a strong H $\alpha$  line in the *I* band ( $\Delta m = 0.14$ ), as well as a combination of a strong H $\beta$  line and prominent Fe II emission in the *R* band ( $\Delta m = 0.11$ ). The removal of flux corresponding to these lines caused a reduction in  $\chi^2/\nu$  of nearly 50% (1.28 – 0.68), without greatly changing the resultant fit, although the fitted synchrotron peak was at a slightly longer wavelength.
- H 1725+044, similarly, has H $\alpha$  in *I* band ( $\Delta m = 0.13$ ) and H $\beta$  + [O III] in *R* band ( $\Delta m = 0.07$ ), and removal of these more than halves  $\chi^2/\nu$  from 2.49 to 1.17, without changing the location of the peak of the synchrotron.
- H 1036–154 has a large Mg II line in the *B* band ( $\Delta m = 0.17$ ), which causes a noticeable upturn in the SED. Removal of this line reduces the  $\chi^2/\nu$  from 0.77 to 0.56, without changing the location of the peak

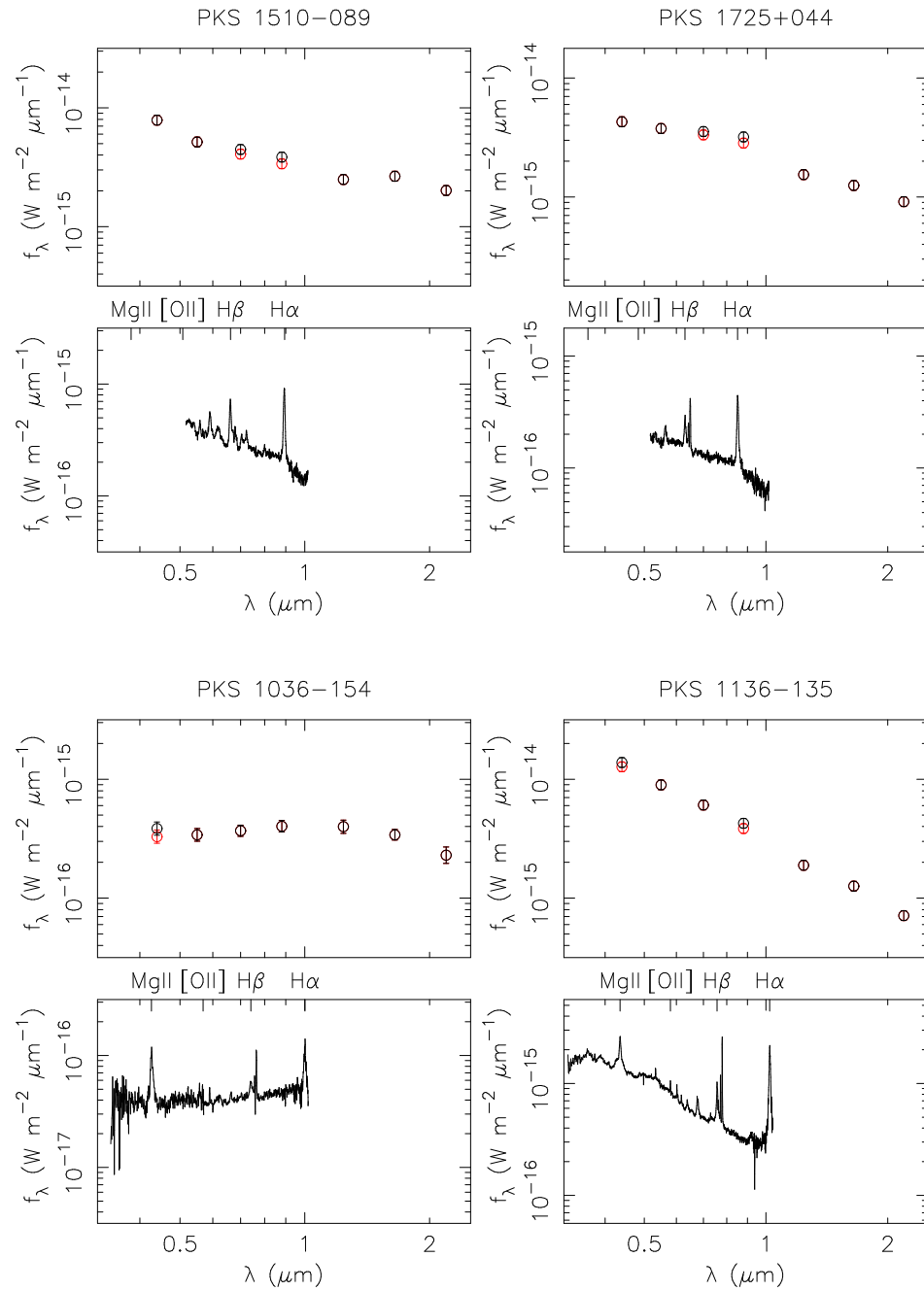


Figure 5.14: The effect of removing strong emission lines from the photometry. The adjusted photometry (as described in the text) is shown in red. The spectra are given for comparison, showing the location of prominent emission lines.

wavelength, although the  $0.5\mu\text{m}$  ratio increases slightly (from 5.3 to 7.2).

- H 1136–135 is initially fit with a pure power law, and this remains the case after removal of the Mg II line ( $\Delta m = 0.09$  in  $B$ ) and both the H $\beta$  and the strong [O III] (total  $\Delta m = 0.11$  in  $I$ ). The power law index softens slightly (from -1.85 to -1.81) and the  $\chi^2/\nu$  value decreases from 0.43 to 0.29.

In conclusion, by selecting quasars with strong emission lines, we have demonstrated that the largest changes to the SED are  $\Delta m \sim 0.25$  in one wave-band. In most cases investigated, removal of the line flux improved the  $\chi^2/\nu$  value of the model fit, but did not significantly alter the nature of the fit. When good quality long-wavelength spectra (preferably at least quasi-simultaneous with the photometry, which is not the case here) are available for these quasars, it should be possible to recalculate the fits, taking the emission line contributions into account, although the general conclusions are not expected to change.

## 5.10 Sources without good fits

Up to this point, we have only discussed the results for the sources with good (i.e. acceptable at the 99% confidence level) fits. A total of 24 sources (or 21 per cent of the total) are not fit well by either the power law model or the combined model. What sort of sources are these?

A few sources ( $\sim 8$ ) have roughly power law SEDs, but with a little curvature ('n'-shaped) in the blue end of the optical. This may be indicative of a small amount of dust attenuation or extinction.

Most of the other sources have one or more photometric points that do not smoothly connect with the rest of the SED. It is possible that, for these points, at least one of the systematic errors discussed in Section 4.5 is dominating, over and above the level that was assigned. In some sources, there may also be further emission processes present that have not been modelled.

